Boosting Green Propellants: The Sustainable Armored Grain for Hybrid Rocket Propulsion

Riccardo Bisin*, Vincenzo Pagliacci* and Christian Paravan*†
*Politecnico di Milano, Aerospace Science and Technology Dept.,
Space Propulsion Laboratory (SPLab)
34, via LaMasa, 20156, Milan, Italy
riccardo.bisin@polimi.it · vincenzo.pagliacci@mail.polimi.it · christian.paravan@polimi.it
†Corresponding author

Abstract

In the last years, the armored grain, a paraffin-based fuel reinforced by a 3D-printed polymeric gyroid-like reinforcement, has been identified as a promising fuel for hybrid rocket engines. In this work, the already promising armored grain concept is improved by developing a greener version. The paraffin wax and the 3D printer polymer to produce for the inner armor are replaced with natural waxes (beeswax and carnauba) and bio-polymers (commercial and in-house produced filaments). The thermal characteristics, mechanical properties at compression, and ballistic responses of the green components and the resulting sustainable armored grain are studied. The brand-new armored grain stands as a high-performance and environment-friendly candidate for hybrid rocket propulsion.

1. Introduction

Hybrid Rocket Engines (HREs) could represent an affordable and effective propulsive alternative to the traditional solid rocket motors (SRMs) and liquid rocket engines (LREs) [1]. In fact, HREs seize the benefits of SRMs and LREs; namely, the reduced cost from the former and the operational flexibility (e.g., thrust modulation) from the latter [2]. The potential of this technology can be exploited by using liquefying fuels, such as paraffin-based formulations, which offer a faster regression rate than conventional polymeric fuels. In this framework, the Space Propulsion Laboratory (SPLab) of Politecnico di Milano is studying paraffin-based formulations to create fuels with high ballistic performance and structural integrity [3]. In the last years, the combination of fast-burning paraffin waxes and 3D-printed reinforcements originates the armored grain [4, 5, 6, 7]. So far, the results attested that armored grains exhibit faster regression rate and higher mechanical performance than traditional "not-armored" paraffin fuels. Several studies have been conducted in the SPLab to explore the armored grain concept. The first investigation focused on the polymeric material for the gryoid reinforcement. Polylactic acid, acrylonitrile butadiene styrene, and nylon 6 were used [6, 7]. The reinforcement was also inspected by changing its volume fraction and its shape. The Schwarz Primitive, and honeycombs with straight and swept channels represented an alternative to the traditional gyroid armor [8]. Lastly, the paraffin matrix impact on the armored grain was examined by using macro- and micro-crystalline waxes in pure and blended form [9]. All the studies highlighted the enhanced structural (ductile behavior and high deformation energy) and ballistic properties (high regression rate) of the armored grain. Is it possible to further improve this already promising new class of fuels?

In recent times there has been a great concern about green propulsion technologies to contrast pollution and climate change. Traditionally, hybrid rockets are addressed to be "environmentally friendly" because of the low pollutant exhausts, if compared to SRMs. The choice of paraffin waxes instead of thermoplastic polymers goes towards HREs with reduced environmental impact. However, paraffins are generally derived from petrolatum. Is it possible to go more sustainable and greener using waxes in HRE? This research targets at empowering the armored grain by developing a greener and more sustainable version. To do this, the two components of the armored grains (i.e, the wax matrix, and the polymer for the inner reinforcement) were modified. More specifically, bio-derived natural waxes were investigated: beeswax and carnauba wax. Similarly, the 3D printer polymeric filament for the gyroid-like reinforcement has been substituted with commercial and in-house produced bio-polymeric filaments. The bio-waxes and the bio-polymers were characterized via thermal analyses, mechanical tests at compression, and firing tests in the lab-scale hybrid rocket motors. The most promising bio-wax and 3D-printed bio-polymeric reinforcements were combined to create a new eco-version of the armored grains. The latter was studied inspecting its mechanical and ballistic behavior to assess its feasibility in HREs and to pave the way to high-performance and more sustainable fuels.

2. Investigated Materials and Fuels

The materials and fuels considered in the present study are classified as waxes, 3D-printer polymers, and armored grains. The first group includes a traditional micro-crystalline paraffin wax (SasolWax-0907), an "insect-derived" wax (Beeswax), a "plant-derived" wax (Carnauba), and a blend of the last two waxes. The 3D printer polymers are the acrylonitrile butadiene styrene (ABS), a commercial bio-polymer (NonOilen), and an in-house produced bio-polymeric filament extruded from pellets of Mater-Bi, a biodegradable material made by Novamont [10]. The 3D printer polymers are used to create the 3D-printed gyroid-like reinforcement for the armored grains.

2.1 Liquefying Fuels: Waxes

The micro-crystalline paraffin wax represents the reference paraffin fuel, which has been widely studied for hybrid rocket propulsion applications [11, 12, 13] in light of its relatively high thermal stability. Two natural substitutes have been identified and studied: beeswax and carnauba.

Micro-Crystalline Wax (mWA). Micro–crystalline paraffin wax (SasolWax-0907) is produced by Sasol GmbH (Germany) [14]. It is composed by 54% branched alkanes (isoalkanes) and 46% linear (n-) alkanes and its average chemical composition is $C_{50}H_{102}$ [12]. SasolWax-0907 features a congealing point between 356-369 K and the density is 928 kg/m^3. In the present work, the nomenclature for the micro–crystalline paraffin wax is mWA.

Beeswax (bWB). Beeswax is a natural wax produced by honey bees to build their honeycomb cells. Chemically, beeswax consists mainly of esters of fatty acids and various long-chain alcohols. Beeswax has been already investigated as liquefying fuel [15, 16, 17, 18, 19] given its good ballistic response, which can be explained by the presence of the oxidizer agent in the average chemical formula ($C_{46}H_{92}O$) [16]. The promising ballistic behavior is counteracted by the low thermal stability (melting point at 333-340 K) and poor mechanical properties. In this work, beeswax has been mixed with a second natural wax (carnauba) to create a natural blend, hereafter called bWD, with increased thermal stability and mechanical properties. The beeswax used in this work is a commercial product. The nomenclature for the beeswax is bWB.

Carnauba Wax (bWC). Carnauba is a wax derived from the leaves of palms belonging to the Copernicia species that are mainly cultivated in South America. This natural wax covers the leaves and buds of the palm, protecting them from the sun and excessive water during the rainy season. The leaves, collected in the dry season, are dried in the sun, then scraped and beaten to peel the wax. Along with thermal protection and water-repellent properties, this wax presents polishing, emollient, thickening, and hardening qualities that make it suitable for cosmetic, pharmaceutical, and restoration (pipes and floors) applications. In the food industry, carnauba is used as a coating agent in confectionery products. Chemically, carnauba is a complex mixture of several compounds, predominantly esters (aliphatic, alpha-hydroxy esters, and cinnamic aliphatic diesters) but also acids, alcohol, and hydrocarbons [20]. From the best knowledge of the authors, this wax has never been used for rocket propulsion applications. The high thermal stability (melting at 353-363 K) and hard mechanical properties make this natural wax a good candidate for sustainable HRE fuel. The carnauba used in this work is a commercial product. The nomenclature for the carnauba is bWC.

2.2 3D Printer Polymers

The Acrylonitrile Butadiene Styrene (ABS) is the reference polymer, which has been studied in open literature as fuel [21, 22, 23] and as the material for the 3D-printed reinforcement of the armored grains [6, 7]. Two bio-polymers have been identified as substitutes for the ABS: the NonOilen (NO) and the Mater-Bi (MB). The former is a commercial bio-polymeric filament, the latter is a bio-polymer in granulate/pellet shape.

Acrylonitrile Butadiene Styrene (ABS). Acrylonitrile butadiene styrene (ABS) is a thermoplastic polymer with good mechanical and thermal properties. The combination of the three monomers gives specific features: styrene provides rigidity, butadiene improves low-temperature toughness, and acrylonitrile augments heat resistance and tensile strength. Thanks to its good mechanical and thermal properties, ABS is commonly employed in FDM, though warping and bed adhesion are troublesome problems during the printing. Moreover, during the printing, ABS filaments emit styrene, which is classified as a possible human carcinogen [24]. The ABS filament is supplied by Prusa [25].

NonOilen (NO).   A commercial bio-filament NonOilen was identified and selected as a "bio-alternative" to the ABS. NonOilen is a biodegradable filament made and provided by Filamentum [26]. It is composed by >35% of polylactic acid (PLA), >55% of polyhydroxy butyrate (PHB), and <10% of natural plasticizer (aliphatic ester). PHB is a polymer belonging to the polyesters class produced by microorganisms and it is biodegradable, as well as bio-derived and compostable [27]. The content of PHB improves the toughness and biodegradability, but it has poor thermal stability. The natural plasticizer increases the processability of the product.

Mater-Bi (MB).   Mater-Bi is a starch-based biodegradable material produced by Novamont, an Italian company active in the bio-plastic field [10]. Novamont has several classes of materials under the trademark of Mater-Bi. They contain thermoplastic starch (TPS) and they differ in the additional components (e.g., polyester, copolyester, cellulose acetate, etc.). The actual composition of the Mater-Bi is not known. Unlike the NonOilen, the Mater-Bi supplied by Novamont is in pellet form. In order to produce a Mater-Bi-based gyroid-like reinforcement for the armored grain, the Mater-Bi filament has to be created from the Mater-Bi pellets. The new in-house SPLab 3D printer Mater-Bi filament was produced via the Felfil filament extrusion system [28]. The system includes the Felfil EVO Extruder and the Felfil Spooler. The former heats up the polymeric pellets to the desired temperature before extruding the material through the nozzle at a certain velocity given by an endless screw. The Felfil Spooler rolls up the filament over a pulley by pulling it with two wheels. The hot filament is cooled thanks to four fans positioned between five metal rings of the Felfil Spooler cooling system. The steps of the filament extrusion procedure can be summarized in the following: parameter setting (extrusion temperature and speed, filament diameter, cooling fan speed), pellets introduction into the heater, manual insertion of the extruded hot filament into the cooling system, the wheels, and pulley to roll up the created filament.

2.3 Investigated Fuels

All the investigated fuels are listed in Table 1. Three are the main categories: polymeric fuels, waxes, and armored grains. The first family includes the "traditional" ABS and the bio-polymer NonOilen. The second family consists of the oil-derived SasolWax-0907 (mWA), the natural insect-derived Beeswax (bWB), the natural plant-derived Carnauba (bWC), and a blend of the last two natural waxes in the 1:1 mass ratio (bWD). All the waxes include 1 wt.% graphite powder black (CB) as an opacifier, in the perspective of their use in ballistic tests. The third family is composed of armored grains based on (i) mWA or bWD, as the wax matrix, and (ii) gyroid-like reinforcements (GY) with different volume fractions (10% and 15%) and made of the 3D printer polymers (ABS, NO or MB). The ABS and NO polymeric fuels are produced via 3D printing (solid print of the final fuel), the waxes via melt-casting procedure[1], and the armored grain via melt-casting of the wax matrix into the 3D-printed polymeric gyroid-like reinforcement (lodged in a cylindrical mold). The selected wax matrices for the armored grains are the mWA and the bWD. The former is the baseline, already tested in previous work [29, 6, 7, 9], the latter is the new bio-wax with good thermal and mechanical properties, as discussed in Sec. 4. Regarding the reinforcement, the gyroids were 3D-printed in ABS, Mater-Bi (MB), and NonOilen (NO). Two typologies of gyroids were studied: the GY_XXX_i10 and the GY_XXX_i15 (refer to Table 1), where XXX relates to the material used for the gyroid (ABS, NO, or MB[2]). The two gyroids feature two different volume fractions (volume of the gyroid divided by the enveloped volume of the entire grain): the GY_XXX_i10 and GY_XXX_i15 series present a 10% and 15% volume fractions (or infills), respectively. Gyroids are created according to the infill gyroid design process [6].

The fuels undergo compression and ballistic tests in the Radial Burning lab-scale hybrid rocket Engine (RBE) and in the Vortex Flow Pancake (VFP), as discussed in Sec. 3. The final dimensions of the fuels are compliant with the testing methodology and setup. The mechanical and ballistic specimens both have cylindrical shapes but present different dimensions. The compression samples are created according to the sizes of the grains fired in the RBE. The specimens for compression and firing tests in the RBE are cylinders with 30 mm external diameter and 50 mm length. Concerning the specimens for the RBE firing tests, a 5 mm hole is also present; this is the initial bore diameter of the single-port, central-perforated cylindrical fuel grain. Differently, the specimens used for the ballistic characterization in the VFP engine are disks with 86 mm diameter and 14 mm height.

3. Methodology

The study of the solid fuels in Table 1 was carried out by investigating the thermal, mechanical, and ballistic behavior. Thermal behaviors of polymers and waxes were inspected via simultaneous thermogravimetry (TGA) and differential thermal analysis (DTA). The mechanical behaviors of waxes, 3D-printed reinforcements, and armored grains were

---

[1]Pure wax is heated above the melting temperature, additives are added and mixed (if needed), the compound is poured inside a specific mold.

[2]The MB-produced gyroids (GY_MB_i10 and GY_MB_i15) are made of the in-house made filament created from the Mater-Bi pellets.

Table 1: Tested fuel formulations and their composition: polymers, waxes, armored grains. The composition of the fuels is expressed in terms of *wt.%* for waxes, while *vol.%* is considered for *armored grains*.

Fuel ID	Category	Composition	Density (TMD), ρ_f, kg/m^3
ABS	3D-printed traditional fuel	100 *wt.%* ABS	1082
NO	3D-printed bio-polymeric fuel	100 *wt.%* NonOilen	1250
mWA	paraffin wax	99 *wt.%* SasolWax-0907, 1*wt.%* CB	929
bWB	bio-Wax (insect-derived)	99 *wt.%* Beeswax, 1*wt.%* CB	905
bWC	bio-Wax (plant-derived)	99 *wt.%* Carnauba wax, 1*wt.%* CB	947
bWD	bio-Wax (blend)	49.5 *wt.%* Beeswax, 49.5 *wt.%* Carnauba, 1*wt.%* CB	996
mWA_GY_ABS_i10	Traditional Armored Grain	90 *vol.%* mWA, 10 *vol.%* ABS (gyroid)	943
mWA_GY_ABS_i15	Traditional Armored Grain	85 *vol.%* mWA, 15 *vol.%* ABS (gyroid)	952
bWD_GY_MB_i10	Sustainable Armored Grain	90 *vol.%* bWD, 10 *vol.%* MB (gyroid)	973
bWD_GY_MB_i15	Sustainable Armored Grain	85 *vol.%* bWD, 15 *vol.%* MB (gyroid)	985
bWD_GY_NO_i10	Sustainable Armored Grain	90 *vol.%* bWD, 10 *vol.%* NO (gyroid)	975
bWD_GY_NO_i15	Sustainable Armored Grain	85 *vol.%* bWD, 15 *vol.%* NO (gyroid)	987

assessed via compression tests. The ballistic responses of 3D-printed fuels, waxes, and armored grains consisted of static firing tests in the radial burning lab-scale HRE (RBE) and the vortex flow pancake (VFP).

3.1 Thermal Characterization

Thermogravimetric analysis (TGA) was performed simultaneously with differential thermal analysis (DTA) to obtain information about the response of the polymers and the waxes (Table 1) to thermal inputs. During the thermogravimetric analysis (TGA), the mass of the specimen is measured as a function of temperature or time while the sample is subjected to a controlled temperature program in a pre-defined atmosphere [30, 31]. In the DTA, the temperature difference between the sample and a reference material is recorded while both of them are subjected to the same heating program. The TGA provides information about the composition and the thermal stability of the sample, the DTA is used to evaluate the melting and crystallization reactions, the solid-solid transition, and the glass transition temperature. Thermal analyses were carried out with a Netzsch STA 449 F5 Jupiter with a vertical weighting system. Tests were performed on ≈ 25 mg samples (nominal mass) under argon (*Ar*) flow (75 ml/min). The temperature range was 298-1273 K with a heating rate of 10 K/min. Degradation onset and end temperatures were evaluated with the tangent method.

3.2 Mechanical Characterization

The structural assessments of the waxes, 3D-printed gyroid reinforcements, and armored grains were carried out via uniaxial compression tests according to ISO 604 [32]. The mechanical tests were conducted on an MTS 858 Mini Bionix II equipped with a 30 KN load cell. The samples are cylinders of 30 mm diameter and 50 mm height. The compression tests were performed at ambient temperature (293 ± 3 K) with a constant compression rate of 1 mm/min. The compression lasts until the sample fractures or the strain reaches the 14.4% predetermined deformation value[3]. At least three samples of each type of specimen were tested. The test campaign provided the stress-strain relationship ($\sigma(\epsilon)$ curve) for the investigated materials and the mechanical properties at compression, such as the Young Modulus (E), the yield point, in terms of yield stress (σ_y) and yield strain (ϵ_y).

3.3 Ballistic Characterization

The ballistic characterization was carried out in the SPLab facilities. The radial burning lab–scale engine (RBE) and the vortex flow pancake motor (VFP) were employed to measure the ballistic response of the fuels, especially the regression rate (r_f). The two setups are illustrated in Fig. 1a and 1b, respectively. Combustion tests with the RBE and the VFP were conducted in gaseous oxygen (OX). The two motors are remotely operated and the experimental setup hardware is based on a National Instruments PXI DAQ. The system is controlled and operated using an in-house developed LabView VI routine.

---

[3]According to ISO 604, the maximum strain achieved during the test should be limited to 14.4% to prevent buckling insurgence.

3.3.1 Radial Burning Engine (RBE)

The RBE (Fig. 1a) is designed to burn single-port, central-perforated cylindrical grains in a vertical configuration. Samples for the firing tests feature the same geometry and size of the ones for the compression tests (Sec. 3.2), with the only difference of an initial central port of 5 mm diameter. The motor features a swirled injection (swirl number S_g equal to 3.3), a pre-combustion chamber lodging the pressure transducer and the ignition system (pyrotechnic igniter), a combustion chamber hosting the fuel grain, a post-combustion chamber and a water-cooled brass nozzle. A quartz window located in the injector head allows the recording of the combustion with a high–speed camera [7]. Firing tests were performed with gaseous oxygen (GOX), whose mass flow rate ($\dot{m}_{ox}$) was regulated by the main flowmeter and kept constant at 5 g/s for the test duration. Hence, the initial oxidizer mass flux (G_{ox}) is ≈ 250 kg/(m^{2}s). The shutdown of the motor was accomplished by closing the OX electrovalves (GOX flow interruption) and by opening the N2 electrovalves (gaseous N2 injection) to quench the flame and purge the system. The pressure trace is used to retrieve the combustion duration $\Delta t_b = t_{end} - t_{in}$, which is essential for the evaluation of the r_f. The t_{in} is the time at which the chamber pressure starts raising. The t_{end} is the time at which the gaseous nitrogen is injected into the combustion chamber to stop the combustion. The burning time was chosen according to the fuel formulation to obtain approximately the same final diameter for all the tested grains, thus the same average oxidizer mass flux ($\bar{G}_{ox}$). According to open literature [33, 34], the $\bar{G}_{ox}$ is the most significant parameter affecting the r_f, so having approximately the same $\bar{G}_{ox}$ is needed to compare the ballistic response of the fuels. The burning time spanned from 4.5 s, for the fastest formulations (i.e., mWA_GY_ABS_i10 and bWD_GY_NO_i10), to 14 s, for the slowest ones (i.e., 3D-printed ABS and NO).

3.3.2 Vortex Flow Pancake (VFP)

The VFP (Fig. 1b) is an engine that is characterized by a combustion chamber delimited by two solid fuel disks. The fuel disks are faced each other and they are separated by a tangential injection ring. The fuels disks dimensions are: 43 mm radius (R_{cc}) and 14 mm height. The initial combustion chamber height is 20 mm (h_{cc}), i.e. the distance between the two disks before the firing. One of the two disks is connected to the engine water-cooled brass nozzle by a central port perforation, in which a tube in carbon fiber (external radius of 12.5 mm) is inserted to prevent the fuel hole from collapsing. The chamber volume increases during the burning time because of the regression of the two fuel disks. The injection ring features four arms to tangentially inject the oxidizer into the chamber and to establish a vortex flow into the combustion chamber. The main flowmeter regulates and supplies the desired oxygen mass flow rate ($\dot{m}_{ox}$) for the test duration. Values of 8-9.5 g/s are typical for the VFP firing tests. The channels of the same injection ring are also used to stop the combustion by nitrogen injection in the chamber. Two channels host the pressure transducer and the pyrotechnic igniter. The nozzle of the VFP engine has a convergent-divergent conical configuration and it is cool down by an enveloped chamber with water flowing inside. The combustion pressure acquisition and the identification of the ignition and shutdown instants enable the evaluation of the burning time Δt_b in the same way as the in the RBE.

3.3.3 Regression Rate Reduction Technique

The solid fuel regression rate (r_f) can be considered one of the most important figure of merit in HREs. The mass-based approach is used evaluate the space-time average regression rate of the solid fuel (r_f) for both the RBE and the VFP firings.

Regression Rate for the RBE. The space-time average regression rate of the solid fuel (r_f) is calculated as the variation of the port diameter that occurs during the firing [34]:

$$r_{f,RBE} = \frac{1}{\Delta t_b} \frac{D(t_{end}) - D(t_{in})}{2} \tag{1}$$

The initial diameter of the fuel port $D(t_{in})$ is ≈ 5 mm. The final diameter $D(t_{end})$ considers the fuel mass variation Δm_f before and after the combustion (weight of the fuel checked before and after the firing):

$$D(t_{end}) = \sqrt{D(t_{in})^2 + \frac{4}{\pi} \frac{\Delta m_f}{\rho_f \cdot L_f}} \tag{2}$$

where ρ_f, and L_f are the density (refer to Table 1) and the initial length (i.e., 50 mm) of the fuel grain, respectively. The average oxidizer mass flux ($\bar{G}_{ox}$) of the test can be estimated by dividing the oxidizer mass flow rate ($\dot{m}_{ox} = 5$ g/s) by the average port area:

$$\bar{G}_{ox,RBE} = \frac{\dot{m}_{ox}}{\frac{\pi}{4} \cdot \left[\frac{D(t_{end}) + D(t_{in})}{2}\right]^2} = \frac{16\dot{m}_{ox}}{\pi[D(t_{end}) + D(t_{in})]^2} \tag{3}$$

5

BISIN, R. ET AL.

Regression Rate for the VFP. Similarly to the RBE, the space-time average regression rate of the solid fuel (r_f) is calculated as the variation of the combustion chamber height (distance between the two disks) that occurs during the firing:

$$r_{f,VFP} = \frac{1}{\Delta t_b} \frac{h_{cc}(t_{end}) - h_{cc}(t_{in})}{2} \tag{4}$$

The initial height of the combustion chamber is $h_{cc}(t_{in})$ is ≈ 20 mm. The final height $h_{cc}(t_{end})$ considers the fuel mass variation Δm_f before and after the combustion (weight of the fuel checked before and after the firing):

$$h_{cc}(t_{end}) = h_{cc}(t_{in}) + \frac{\Delta m_f}{\rho_f \cdot A_f} \tag{5}$$

where A_f is the total (flat burning) surface of the two fuel disks. The average oxidizer and total mass fluxes ($\bar{G}_{ox}$ and $\bar{G}_{tot}$) are computed taking into account an average combustion chamber height:
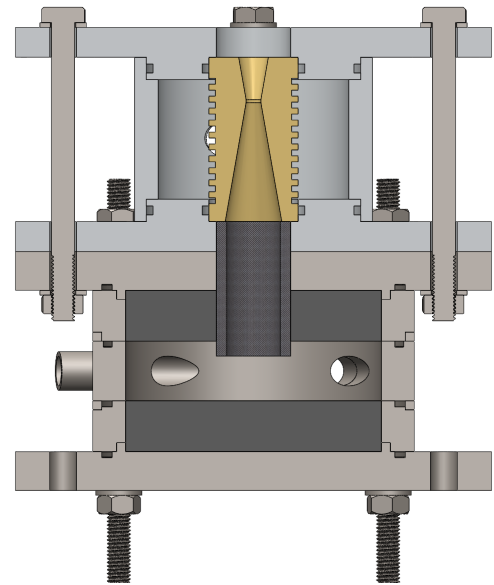
$$\bar{G}_{ox,VFP} = \frac{\dot{m}_{ox}}{R_{cc} \cdot \bar{h}_{cc}} = \frac{2\dot{m}_{ox}}{R_{cc} \cdot [h_{cc}(t_{in}) + h_{cc}(t_{in})]} \tag{6}$$

$$\bar{G}_{tot,VFP} = \frac{\dot{m}_{ox} + \dot{m}_f}{R_{cc} \cdot \bar{h}_{cc}} = \frac{2(\dot{m}_{ox} + \dot{m}_f)}{R_{cc} \cdot [h_{cc}(t_{in}) + h_{cc}(t_{in})]} \tag{7}$$

where R_{cc}, the chamber radius, is constant at 43 mm during the firing.
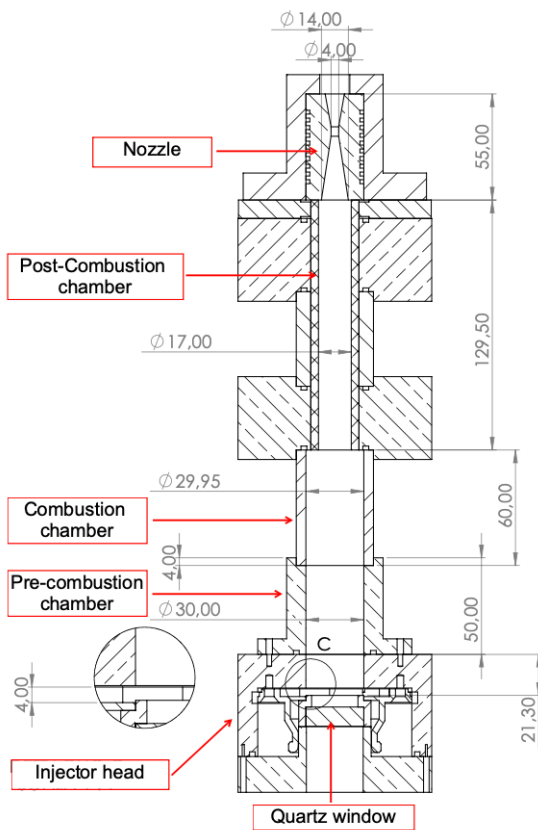
(a) Radial Burning Engine (RBE) [7].

(b) Vortex Flow Pancake (VFP) [35].

Figure 1: Schematics of the SPLab lab-scale hybrid rocket motors: (a) RBE, (b) VFP.

4. Results and Discussion

4.1 Thermal Behavior

The thermal analysis results are reported hereafter for the waxes and the 3D printer polymers.

4.1.1   Waxes

The thermal traces of paraffin and natural waxes are depicted in Fig. 2a and Fig. 2b, while the relevant quantities are summarized in Table 2. The reference mWA paraffin wax feature a wide endothermic process spanning from 325.6 K to 392.7 K, indicating the presence of various hydrocarbons (including n-alkanes, iso-alkanes and cycloalkanes) with different molecular weights and melting temperatures. The paraffin wax mWA exhibits the highest $T_{end,m}$ among the waxes. The bWC shows a 21 K higher melting peak with respect to bWB because of the higher molecular weight of the components of the former wax. Indeed, bWB and bWC consist predominantly of straight aliphatic esters, in particular esters of long-chain fatty acids and long-chain alcohols compounds [20]. However, the main ester of bWB is made of palmitic acid (C_{16}) and 1–triacontanol (C_{30}), while the 40% components of bWC predominantly derive from acids and alcohols in the higher C_{26}-C_{32} range [20]. The higher molecular weight of the specimens components reflects also in higher degradation onset and end temperatures, being the mWA the most thermally stable material (Table 2, Fig. 2b). The onset and end degradation temperatures of bWC are respectively 669 K and 726 K, and the bWC is the wax with the closest degradation temperature range to the mWA. The bWB shows a 85 K lower $T_{on,deg}$ than bWC, while only 41 K difference distinguishes the $T_{end,deg}$ of the two natural waxes. All the investigated fuels degrade at $\approx 100\%$, since no residual masses at $T > 873$ K are detected. The bWD shows an intermediate thermal behavior with respect to pristine single components (bWB and bWC). This holds for all the thermal parameters.
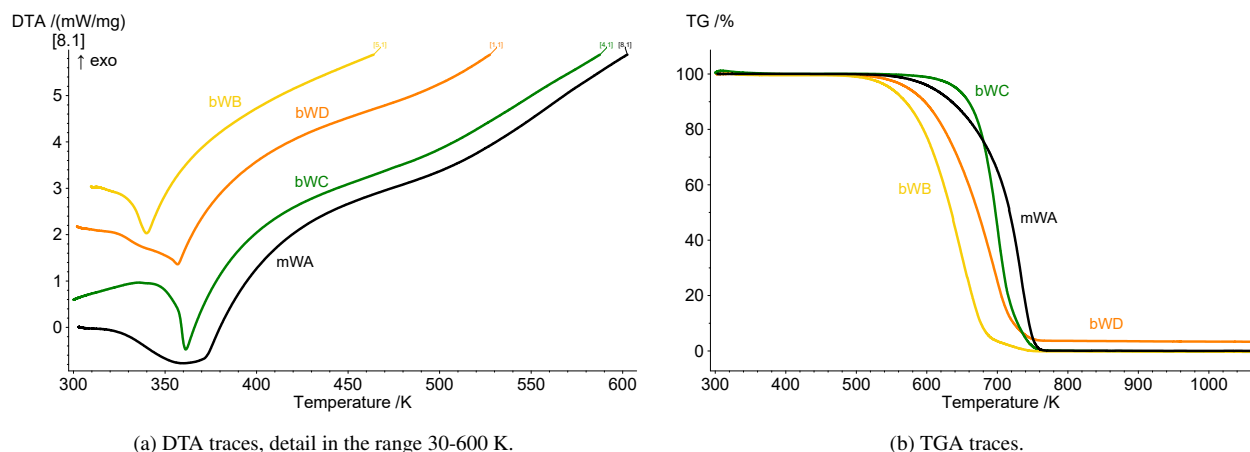

(a) DTA traces, detail in the range 30-600 K.

(b) TGA traces.

Figure 2: Slow heating rate behavior of the investigated waxes (10 K/min, 75 ml/min Ar, 25.0 ± 1 mg).

Table 2: Thermal analysis results of the investigated waxes (10 K/min, 75 ml/min Ar, 25.0 ± 1 mg).

Specimen	Melting onset temperature, $T_{on,m}$ [K]	Melting peak temperature, $T_{peak,m}$ [K]	Melting end temperature, $T_{end,m}$ [K]	Degradation onset temperature, $T_{on,deg}$ [K]	Degradation end temperature, $T_{end,deg}$ [K]	Mass loss (373-873K) $\Delta m_{373-873}$ [%]
mWA	325.6	360.2	392.7	688.7	750.5	99.9
bWB	326.9	339.8	351.9	584.2	684.3	-99.9
bWC	352.8	361.3	380.9	669.3	725.7	≈ 100
bWD	341.1	356.8	367.2	621.8	722.8	-96.4

BISIN, R. ET AL.

4.1.2 3D Printer Polymers

The thermal traces of 3D printer polymers are depicted in Fig. 3a and Fig. 3b, while the relevant thermal properties are summarized in Table 3. Differently from the waxes, the DTA traces of polymers potentially indicate an additional observable parameter to the melting temperatures: the glass transition temperature (T_g). In the DTA signal, the T_g is observed as a jump in the signal baseline pointing downwards. Among the polymers, only ABS exhibits a (faint) T_g at 381.4 K. The NonOilen filament consists of PLA (%35), PHB (%55) and natural plasticizer (%10) [26]. The semi-crystalline nature of NO filament is evinced by the melting peak at 445.6 K, which belongs to the typical PHB melting domain [36]. The melting process of PLA is not visible, probably because of the combined effect of plasticizer and the crossed melting ranges of PLA and PHB. No clear endothermic peaks are observed for the Mater-Bi, whose glassy state could be found at lower temperatures than the ambient one [37]. The thermogravimetric behaviors of the polymers in Fig. 3b and Table 3 attest the lower thermal stability of NonOilen (NO), whose TGA reveals a two-stage degradation process, which testifies the presence of the two main constituents of NonOilen. The first step of mass loss is attributed to the degradation of PHB, while the second to PLA [38]. Black ash, which was present in the DTA/TGA crucible after the analysis and probably related to the plasticizer agent, explains the remaining percentage mass at 873 K ($\Delta m_{373-873}$) of 4.4%. The MB does not present a multiple-step degradation process, suggesting the presence of a single component forming the Mater-Bi. Generally, the degradation processes of the polymers occur in the same temperature range as the waxes. Hence, all the polymers are suitable for the realization of the armored grain. In fact, having the degradation processes of polymers and waxes in the same temperature range is deemed to guarantee the contemporary burning of both components of armored grain (3D-printed gyroid and the surrounding wax matrix) and to avoid anisotropic combustion.
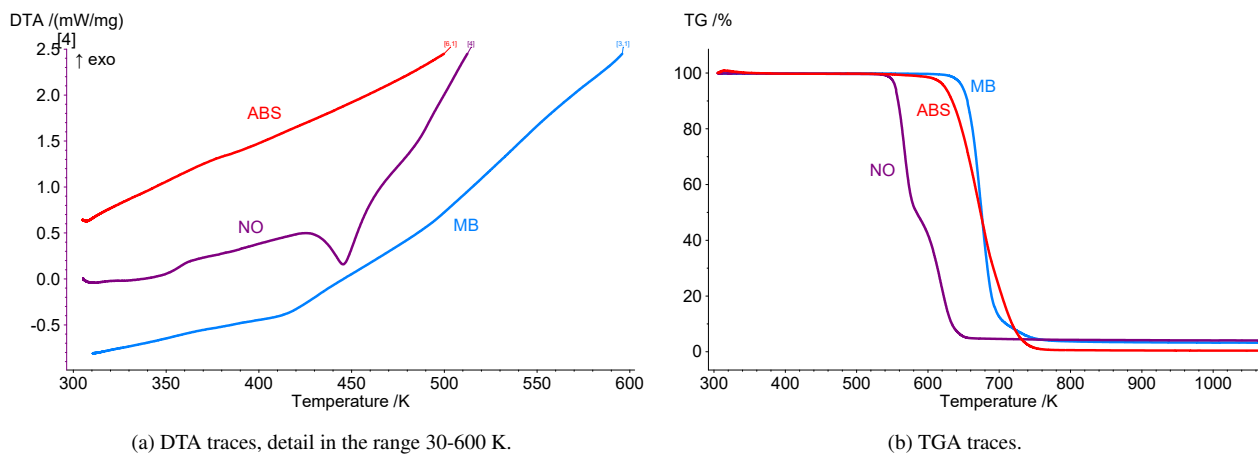

(a) DTA traces, detail in the range 30-600 K.

(b) TGA traces.

Figure 3: Slow heating rate behavior of the 3D printer polymers (10 K/min, 75 ml/min *Ar*, 25.0 ± 1 mg).

Table 3: Thermal analysis results of the investigated 3D printer polymers (10 K/min, 75 ml/min *Ar*, 25.0 ± 1 mg). Note: MB results refer to the raw material in pellet form provided by Mater-Bi.

Specimen	Glass transition temperature, T_g [K]	Melting onset temperature, $T_{on,m}$ [K]	Melting peak temperature, $T_{peak,m}$ [K]	Melting end temperature, $T_{end,m}$ [K]	Degradation onset temperature, $T_{on,deg}$ [K]	Degradation end temperature, $T_{end,deg}$ [K]	Mass loss (373-873K) $\Delta m_{373-873}$ [%]
ABS	381.4	-	-	-	633.5	714.2	-99.5
MB	-	-	-	-	656.1	693.2	-96.5
NO	-	431.4	445.6	460.1	553.8	637.3	-95.6

4.2 Compression Test Results

The compression test results are reported hereafter for the waxes, the 3D-printed gyroid-like reinforcements, and the armored grains.

4.2.1 Waxes

The mechanical responses at compression of the waxes are illustrated in Fig. 4 in terms of (average) stress-strain curves and the mechanical properties listed in Table 4, where the Young Modulus (E) and the yield point (σ_y and ϵ_y) are reported. The different nature of the waxes leads to different mechanical properties with carnauba (bWC) exhibiting an exceptionally strong (σ_y) and stiff behavior (E). The σ_y and E are respectively 4.3 and 2.8 times greater than those of the mWA, which is considered the reference wax. The bWC withstands loads up to 15 MPA, a value that is almost 15 times larger than the σ_y of bWB. Nevertheless, the extremely brittle behavior of bWC is highlighted by the 1.84% yield strain, which corresponds to the strain at break, and it is also testified by the sudden stress drop in the $\sigma(\epsilon)$ curve. On the contrary, the mechanical behavior of bWB is characterized by an elastoplastic response typical of ductile materials. Thus, the yield point of bWB does not coincide with the failure point and the elastic region of the stress-strain curve is followed by a plastic deformation. Indeed, the mechanical properties of the co-blend bWD show intermediate values between those of the bWB and bWD, with σ_y=7.18 MPa and E=642 MPa.

Table 4: Mechanical properties at compression: waxes (compression rate 1 mm/min, testing temperature 293 ± 3 K). Ensemble average values derived by at least three runs for each sample.

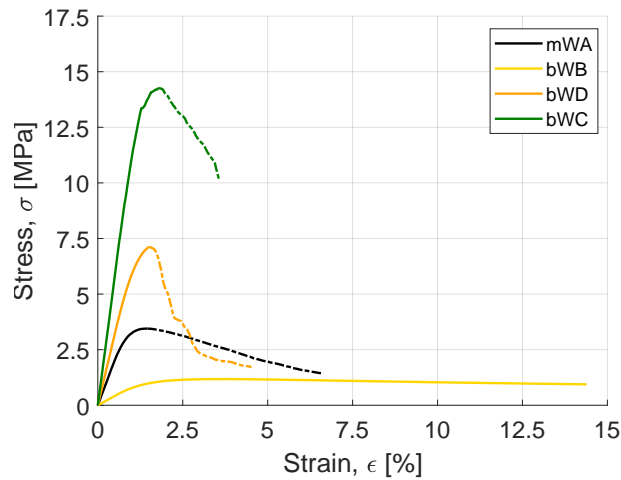| Specimen	Young Modulus, E [MPa]	Yield stress, σ_y [MPa]	Yield strain, ϵ_y [%]
mWA	407 ± 18	3.46 ± 0.13	1.47 ± 0.05
bWB	84 ± 15	1.18 ± 0.08	3.60 ± 0.31
bWC	1152 ± 44	15.01 ± 0.73	1.84 ± 0.37
bWD	642 ± 42	7.18 ± 0.33	1.60 ± 0.15

Figure 4: Engineering stress-strain curves at compression: waxes (ensemble average curves derived by at least three runs for each sample, compression rate 1 mm/min, testing temperature 293 ± 3 K). Note: each average curve is traced as a solid line from the test start to the failure point, while a dashed line is used from the latter point on.

4.2.2 Polymeric Reinforcing Structures

The mechanical responses at compression of the 3D-printed gyroids (infill 10% and 15%) are illustrated in Fig. 5 in terms of (average) stress-strain curves. The mechanical properties are listed in Table 5, where the Young Modulus (E) and the yield point (σ_y and ϵ_y) are reported. As a general consideration, the gyroids do not experience any brittle fracture collapse, and they respond to compression by crumpling constantly and homogeneously. The stresses after the yield point do not show a sudden drop, instead, they settle to a sort of plateau value. Two factors dominate the mechanical properties of the gyroids: the volume fraction (infill or relative density) and the properties of the bulk material. Focusing on the first aspect (contrast GY_XXX_i10 with GY_XXX_i15 specimens), lower infill implies lower mechanical properties (stress at yield and Young Modulus). The 15% infill gyroids (GY_XXX_i15) exhibit

BISIN, R. ET AL.

$\Delta E \approx 59 - 218\%$ and $\Delta\sigma_y \approx 106 - 243\%$ with respect to the 10% infill counterparts (GY_XXX_i10). ABS-based gyroids are the most sensitive to the infill variation. Focusing on the different 3D printer polymers, the mechanical properties of the gyroids made by the in-house MB-produced filament are one order of magnitude lower than the ones of the ABS- and NO-gyroids. Commercial filaments provide the gyroids with stronger and stiffer behaviors. In particular, NO-based gyroids present the stiffest and strongest response. The MB-based gyroids exhibit a very soft response to compression, and the specimens after the compression tests show an elastic return to their uncompressed shape. This feature explains the typical commercial application of Mater-Bi for stretch-demanding uses, such as bags for heavy-weight goods and plastic films. On the contrary, the ABS- and NO-gyroids display struts fracture during the compression tests.

Table 5: Mechanical properties at compression: 3D-printed gyroids (compression rate 1 mm/min, testing temperature 293 ± 3 K). Ensemble average values derived by at least three runs for each sample.

Specimen	Young Modulus, E [MPa]	Yield stress, σ_y [MPa]	Yield strain, ϵ_y [%]	Lattice density, ρ [g/cm^3]
GY_ABS_i10	15.5 ± 0.7	0.46 ± 0.03	6.59 ± 0.60	0.118 ± 0.001
GY_ABS_i15	48.7 ± 1.3	1.58 ± 0.03	5.11 ± 0.35	0.165 ± 0.001
GY_MB_i10	1.6 ± 0.1	0.08 ± 0.01	6.33 ± 0.92	0.136 ± 0.002
GY_MB_i15	2.8 ± 0.1	0.18 ± 0.01	8.84 ± 0.52	0.190 ± 0.008
GY_NO_i10	46.8 ± 1.3	0.92 ± 0.04	2.82 ± 0.06	0.137 ± 0.001
GY_NO_i15	74.5 ± 5.5	1.90 ± 0.06	5.01 ± 0.27	0.194 ± 0.001

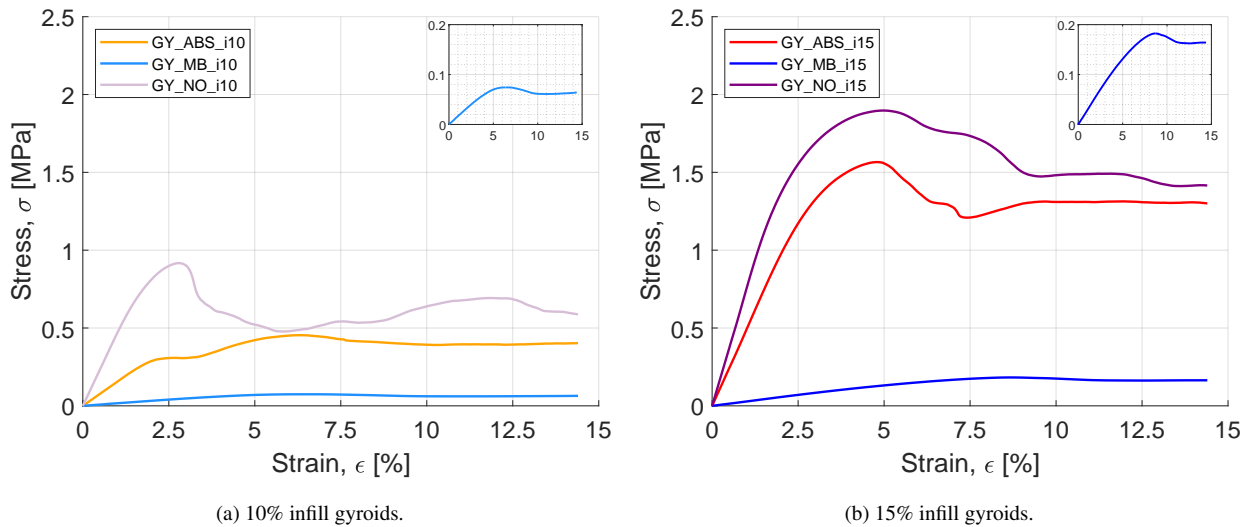(a) 10% infill gyroids.

(b) 15% infill gyroids.

Figure 5: Engineering stress-strain curves at compression: 3D-printed gyroids (ensemble average curves derived by four runs for each sample, compression rate 1 mm/min, testing temperature 293 ± 3 K).
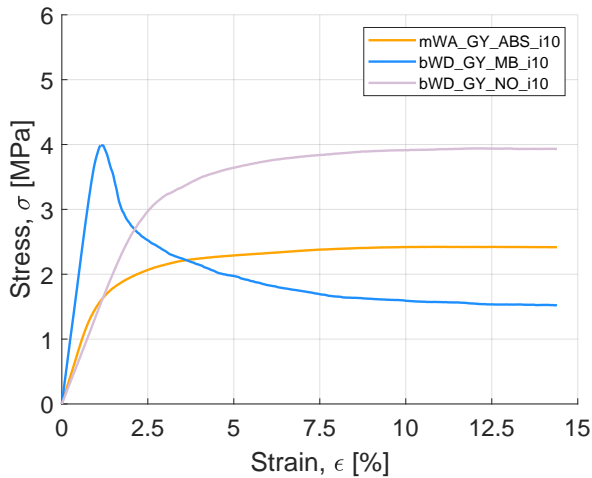
4.2.3 Armored Grains

The mechanical responses at compression of the armored grains featuring the different gyroid reinforcements (infill 10% and 15%) are illustrated in Fig. 6 in terms of (average) stress-strain curves. The mechanical properties are listed in Table 6, where the Young Modulus (E) and the yield point (σ_y and ϵ_y) are reported. As a general consideration, the presence of a gyroid-like reinforcement is able to provide the brittle paraffin matrix (mwA or bWD depending on the considered armored grain family) with a ductile behavior, as testified by the plateau stress achieved by all the armored grains during compression tests. This is the real breakthrough of the armored grain concept: overcoming the intrinsic brittleness of waxes, providing them with a plastic field and with enhanced deformation energy. During the compression tests, the armored grains form wax slivers and chunks, but the grains do not crack in a frail way. Indeed, the mechanical properties of the armored grains are the result of (i) the selected wax for the matrix (mwA or bWD), (ii) the material used to 3D print the gyroid reinforcement, and (iii) the infill fraction of the chosen gyroid (10% or

15%). The choice of the wax mainly affects the maximum allowable stress. The stronger behavior of the bWD-based armored grains than the mWA-based ones (bWD_GY_XXX_iYY vs mWA_GY_ABS_iYY) is related to the higher σ_y of bWD than mWA. Surprisingly, the armored grains reinforced by gyroids in MB (the softest material, refer to Table 5) experience the stiffest behavior. The gyroid-paraffin interface could be the location for the crack onet and the detachment of wax chunks from the inner armor. A soft reinforcement (e.g. MB-based gyroid), rather than a stiff one (e.g. NO-based gyroid), could have a positive impact on the stiffness of the resulting armored grain. The MB-based armored grains present plateau stresses lower than the yield stress, as a consequence of wax matrix failure and the very low strength value the MB-gyroids can withstand (0.8 MPa and 0.18 MPa for GY_MB_i10 and the GY_MB_i15, respectively). Conversely, the ABS- and NO-based armored grains are characterized by the yield stresses coinciding with the plateau stresses. A small deviation of the plateau stress from the σ_y is experienced for bWD_GY_NO_i15. Comparison between Figs. 6a and 6b corroborates the evidence that gyroids with higher infills are preferable to achieve enhanced mechanical properties, as observed in previous studies [6, 29, 9],

Table 6: Mechanical properties at compression: armored grains (compression rate 1 mm/min, testing temperature 293 ± 3 K). Ensemble average values derived by four runs for each sample.

Specimen	Young Modulus, E [MPa]	Yield stress, σ_y [MPa]	Yield strain, ϵ_y [%]
mWA_GY_ABS_i10	171 ± 18	2.42 ± 0.04	≈ 15
mWA_GY_ABS_i15	212 ± 22	3.66 ± 0.18	≈ 15
bWD_GY_MB_i10	379 ± 46	4.01 ± 0.62	1.15 ± 0.04
bWD_GY_MB_i15	406 ± 40	4.65 ± 0.32	1.53 ± 0.06
bWD_GY_NO_i10	136 ± 15	3.95 ± 0.11	≈ 15
bWD_GY_NO_i15	232 ± 16	4.99 ± 0.16	5.66 ± 1.24

(a) 10% infill gyroid-based armored grains.
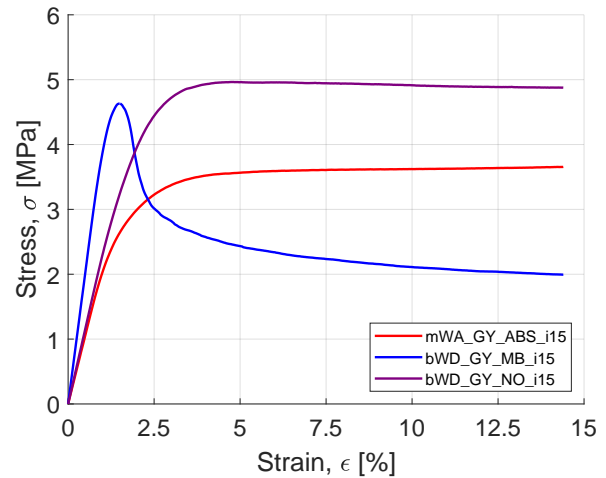
(b) 15% infill gyroid-based armored grains.

Figure 6: Engineering stress-strain curves at compression: armored grains (ensemble average curves derived by four runs for each sample, compression rate 1 mm/min, testing temperature 293 ± 3 K).

4.3 Ballistic Response

The ballistic performances of 3D-printed polymeric fuels, waxes, and armored grains were investigated via the radial burning engine (RBE) and the vortex flow pancake (VFP). The closeness of the $\bar{G}_{ox}$ values allows the comparison of the ballistic performance under approximately the same operating conditions. Figures 7 and 8 illustrate the specimens after the firing tests. The figures highlight the characteristic rough burning surfaces of armored grain (Figs. 7b and 8b) and the rippled burning surface of the VFP wax grain induced by the vortex flow inside the VFP combustion chamber (Fig. 8a).

(a) Wax.

(b) X-ray tomography of armored grain (the wax matrix is in dark gray, the gyroid in light gray).
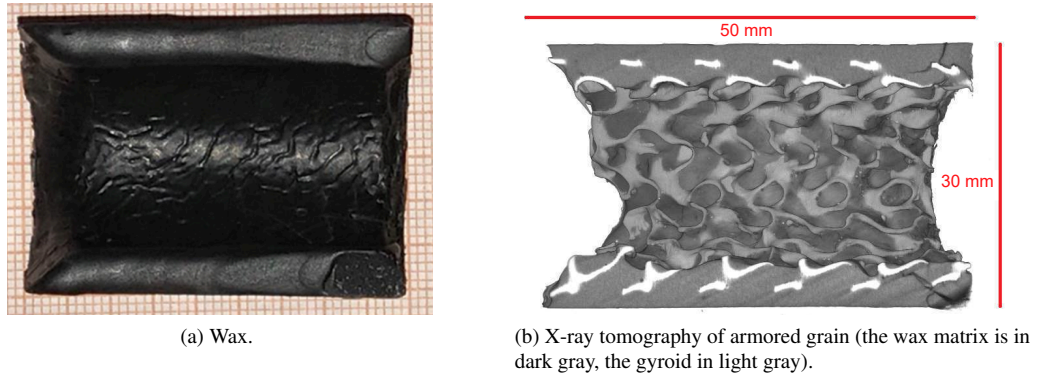
Figure 7: RBE fuel samples after the firing tests: cross-sectional view of wax and armored grain. The oxidizer is direct rightward. [7].

(a) Wax.

(b) Armored grain [39].

Figure 8: VFP fuel disks after the firing tests. The grains are those of the VFP nozzle side (upper disk in Fig. 1b). Disks dimensions are: 43 mm external radius, 12.5 mm internal radius.

4.3.1 RBE Burning Tests

The results of the static firing tests in the RBE are summarized in Table 7. For each type of fuel, three tests were carried out under the same operating conditions (i.e., same $\bar{G}_{ox}$). Figures 9 and 10 illustrate the $r_f(G_{ox})$ values of Table 7 for all the investigated formulations. For the sake of completeness and to make an easier comparison, the $r_f(G_{ox})$ power law fitting of mWA based on an additional data set is present in the figures.

Table 7: RBE ballistic results of all the investigated fuels: polymeric fuels, waxes, and armored grains. Test conditions: initial fuel port diameter of 5 mm, $\dot{m}_{ox}$ = 5 g/s, and nozzle throat diameter of 5 mm, except where otherwise stated.

Specimen	Mean pressure, $\bar{P}_c$ [MPa]	Fuel mass flow rate, $\dot{m}_f$ [g/s]	Average oxidizer mass flux, $\bar{G}_{ox}$ [kg/(m²)s]	Regression rate, r_f [mm/s]
ABS[a,b]	0.86 ± 0.06	0.96 ± 0.09	42.8 ± 4.4	0.47 ± 0.04
NO	0.34 ± 0.05	0.78 ± 0.05	43.2 ± 1.2	0.34 ± 0.02
mWA[a]	0.85 ± 0.09	2.32 ± 0.11	36.3 ± 1.4	1.21 ± 0.04
bWB	0.55 ± 0.02	2.77 ± 0.03	33.8 ± 1.5	1.42 ± 0.04
bWC	0.51 ± 0.01	2.27 ± 0.10	43.2 ± 2.5	1.18 ± 0.09
bWD	0.51 ± 0.02	2.39 ± 0.21	37.4 ± 1.1	1.27 ± 0.03
mWA_GY_ABS_i10[a]	0.57 ± 0.01	4.77 ± 0.14	29.1 ± 1.1	2.23 ± 0.13
mWA_GY_ABS_i15[a,b]	0.86 ± 0.05	3.69 ± 0.10	36.0 ± 0.7	1.87 ± 0.04
bWD_GY_MB_i10	0.65 ± 0.08	3.60 ± 0.36	37.2 ± 2.2	1.82 ± 0.11
bWD_GY_MB_i15	0.59 ± 0.05	3.20 ± 0.19	36.1 ± 1.2	1.57 ± 0.07
bWD_GY_NO_i10	0.56 ± 0.03	4.63 ± 0.39	29.5 ± 2.6	2.07 ± 0.01
bWD_GY_NO_i15	0.52 ± 0.02	3.39 ± 0.21	34.9 ± 1.9	1.62 ± 0.08

[a] From Ref. [7].
[b] Nozzle throat diameter of 4 mm.

The results confirm the faster burning behavior of liquefying fuels (waxes) with respect to polymeric fuels (ABS and NO), which only undergo pyrolisis/vaporization processes and not entrainment. Among the polymeric fuels, the NonOilen (NO) burns slower than the ABS of $\approx$ 27%. The $r_f(G_{ox})$ fitting law of mWA in Fig. 9 enables a comparison of the different waxes with respect to the reference mWA at the same $\bar{G}_{ox}$. The bWB has a better ballistic response than the mWA, whose regression rate is close to the one of the bWD. Carnauba (bWC) is the wax with the lowest r_f. In general, higher thermal stability and mechanical properties are correlated to the higher viscosity of the melted fuel. Therefore, the lower regression rate of bWC could be associated with the higher melted fuel viscosity than bWB. A rheological analysis would be performed to inspect the viscosity of the different fuels.

The individual components of the investigated armored grains (polymeric reinforcement and wax matrix) feature different ballistic performances: the wax (bWD or mWA) burns 2.5-to-4 times faster than the polymer (ABS or NO) used for the inner reinforcement. Nevertheless, the r_f values of the armored grains are not in between their components: the armored grains outperform both the polymeric fuels and the waxes, as shown in Fig. 10. This result is in agreement with the open literature about armored grain [7] and it can be explained by the rough burning surface generated during combustion (refer to Fig. 7b), in turn, increasing the skin friction coefficient, the turbulence level, and the heat feedback to the fuel surface. Focusing on bio-armored grain with the 15% infill gyroids (Fig. 10b and Table 7), the r_f values of MB- and NO-based armored grains (bWD_GY_MB_i15 and bWD_GY_NO_i15) show +24% and +28% increments with respect to bWD, respectively. A more significant difference between the two bio-armored grains is experienced when comparing the fuels reinforced by 10% infill gyroids. The use of the 10% infill gyroids leads to r_f increments with respect to bWD of +44% (bWD_GY_MB_i10) and +63% (bWD_GY_NO_i10). This evidences (i) the positive impact of lightweight gyroids (i.e., low infill), and (ii) the effect of the material used for the gyroid production. The faster ballistic response of NO-armored grains than the MB-armored grains could be explained by the higher thermal stability of the former bio-polymer (refer to Tab. 3).

Despite the comparable burning behavior of bWD and mWA (r_f=1.27 mm/s at $\bar{G}_{ox}$=37.4 kg/(m²s), r_f=1.21 mm/s at $\bar{G}_{ox}$=36.3 kg/(m²s), respectively), the results in Table 7 and Fig. 10 highlight the higher r_f of the ABS-based armored grains than the corresponding bio-armored grain versions based on MB and NO. Once again, the influence of the polymer on the r_f is remarked: the faster the polymer for the gyroid (ABS with respect to NO, as shown in Fig. 9), the faster the corresponding armored grain. Armored grains with 10% and 15% ABS infill gyroids (mWA_GY_ABS_i10 and mWA_GY_ABS_i15) show Δr_f of +8% and +15% with respect to the NO counterparts (bWD_GY_NO_i10 and bWD_GY_NO_i15), respectively.
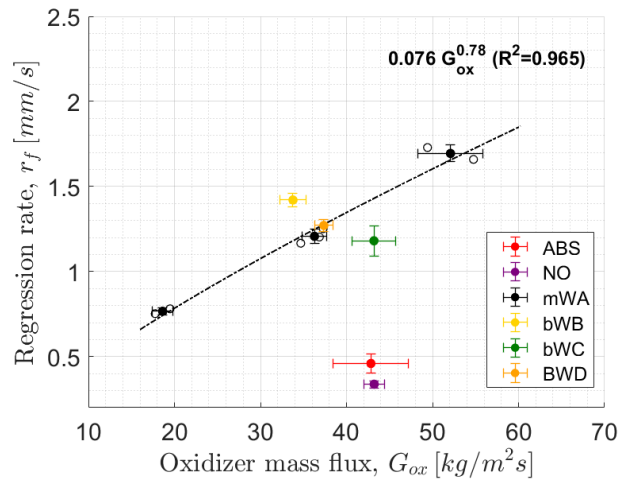
Figure 9: RBE ballistic results: $r_f(G_{ox})$ for the investigated waxes and the 3D printer polymers. Circles with error bars are the average r_f, as reported in Table 7 (additional results are shown for mWA). Note: the $r_f(G_{ox})$ power law fitting for the mWA fuel is also present.

(a) 10% infill gyroid-based armored grains.

(b) 15% infill gyroid-based armored grains.
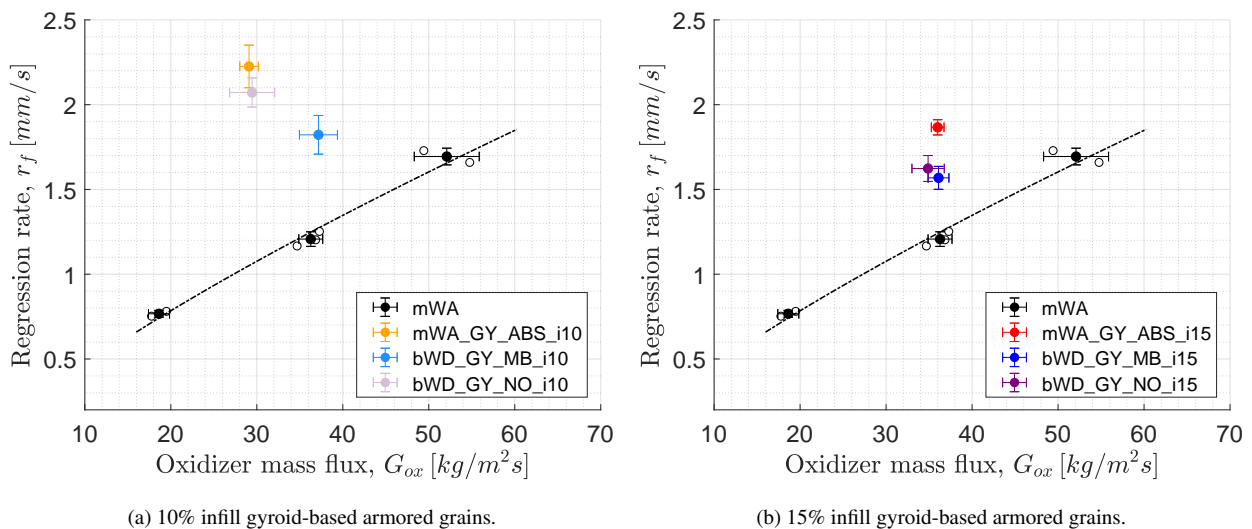
Figure 10: RBE ballistic results: $r_f(G_{ox})$ for armored grains. Circles with error bars are the average r_f, as reported in Table 7 (additional results are shown for mWA). Note: results and $r_f(G_{ox})$ power law fitting for the mWA are also present.

4.3.2 VFP Burning Tests

The results of the static firing tests in the VFP are summarized in Table 8. The test campaign is limited to four different formulations, each one representing a different fuel category (as listed in Table 1): the ABS for the 3D-printed fuel group, the mWA for the waxes (i.e. fast-burning fuels undergoing entrainment phenomenon), and mWA_GY_ABS_i10 and bWD_GY_MB_i10 for the armored grains in the "traditional" and "sustainable" version. Armored grains featuring 10% gyroid reinforcements have been preferred to the 15% counterpart because of the higher performances in terms of r_f evinced by the RBE characterization. For each type of fuel, at least two tests were carried out under approximately the same operating conditions (i.e., same $\bar{G}_{ox}$). Figure 11 illustrates the $r_f(G_{ox})$ of Table 8 for all the investigated formulations. For the sake of completeness and to make an easier comparison, the $r_f(G_{ox})$ power law fitting of mWA based on an additional data set is also present.

Table 8: VFP ballistic results of ABS (polymeric fuel), mWA (paraffin wax), mWA_GY_ABS_i10 and bWD_GY_MB_i10 (armored grains).

Specimen	Burning time, Δt_b [s]	Mean pressure, $\bar{P}_c$ [MPa]	Oxidizer / fuel mass flow rate, $\dot{m}_{ox}$ [g/s]	$\dot{m}_f$ [g/s]	Average oxidizer / total mass flux, $\bar{G}_{ox}$ [kg/(m^{2}s)]	$\bar{G}_{tot}$ [kg/(m^{2}s)]	Regression rate, r_f [mm/s]
ABS	15.4 ± 0.1	0.85 ± 0.01	8.00 ± 0.01	2.60 ± 0.05	8.08 ± 0.01	10.70 ± 0.03	0.23 ± 0.01
mWA	8.5 ± 0.7	1.36 ± 0.02	9.50 ± 0.01	7.73 ± 0.52	8.85 ± 0.04	16.05 ± 0.52	0.78 ± 0.05
mWA_GY_ABS_i10	8.2 ± 1.5	1.36 ± 0.03	9.00 ± 0.01	9.88 ± 0.15	8.13 ± 0.22	17.06 ± 0.61	0.99 ± 0.03
bWD_GY_MB_i10	5.5 ± 0.8	1.28 ± 0.01	9.50 ± 0.01	9.25 ± 0.96	9.28 ± 0.05	18.32 ± 1.03	0.85 ± 0.09

Table 8 and Fig. 11 confirm the fast-burning behavior of mWA with respect to ABS, as already pointed out by the RBE burning tests. Additionally, the characteristic vortex promoted by the VFP seems to further improve the ballistic response of liquefying fuels: in the VFP, the r_f of mWA is 3.4 times greater than the r_f of ABS, while in the RBE a 2.5 times increment was experienced.

The fast-burning behavior of mWA can be further enhanced by 27% when embedding the GY_ABS_i10 gyroid (contrast mWA with mWA_GY_ABS_i10). The ballistic characterization using the VFP confirms the higher r_f of the ABS-reinforced armored grain with respect to its bio version bWD_GY_MB_i10. The latter fuel performs better than the mWA wax, but lower r_f increments are achieved in the VFP than in the RBE. In general, the armored grain concept is more attractive in the RBE than in VFP, since higher Δr_f increments with respect to the not-armored formulations are observed in the former engine. This can be related to the different engine configurations and the different internal flow fields of the RBE and the VFP. Indeed, the presence of the 3D-printed structure alters the burning surface, which is extremely rough, as shown in Fig. 8b. However, the armored grain concept seems to be less effective in the already highly turbulent vortex flow field generated by the swirl injection of the VFP. The intense vortex inside the VFP is testified by the rippled wax fuel grain in Fig. 8a.
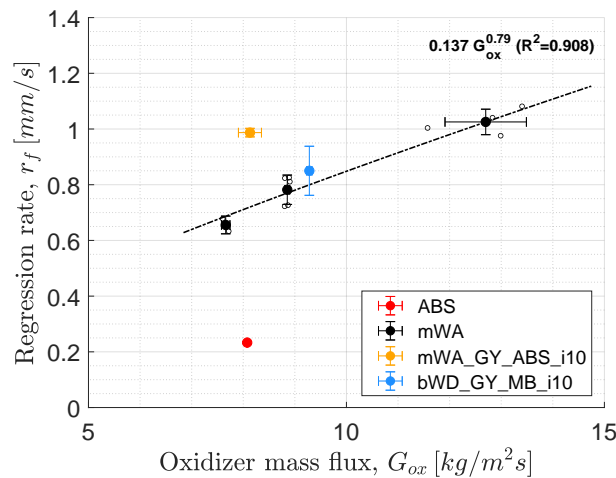

Figure 11: VFP ballistic results: $r_f(G_{ox})$ for mWA, ABS, mWA_GY_ABS_i10, and bWD_GY_MB_i10. Circles with error bars are the average r_f, as reported in Table 8 (additional results are shown for mWA). Note: the $r_f(G_{ox})$ power law fitting for the mWA fuel is also present.

5. Conclusion and Future Developments

The armored grain, a heterogeneous fuel composed by a 3D-printed gyroid structure embedded in a surrounding wax matrix, was studied to develop a more sustainable and "eco-friendly" version. To do this, the two components of the armored grains (i.e, the paraffin matrix, and the polymer for the inner reinforcement) were substituted with greener ingredients. Bio-derived natural waxes were chosen to replace the traditional micro-crystalline oil-derived paraffin wax (mWA): the insect-derived beeswax (bWB) and the plant-derived carnauba (bWC). A 1:1 mass ratio blend of the last two bio-waxes, the bWD wax, was also investigated. Coherently, the traditional ABS used for the 3D-printed gyroid reinforcement of the armored grain was replaced with two bio-polymers: a commercial filament (NO) and in-house produced bio-polymeric filament from pellets of Mater-Bi (MB).

The bio-waxes and the bio-polymers were characterized via thermal analyses, mechanical tests at compression, and firing tests in the conventional lab-scale hybrid rocket motor (RBE) and in the innovative vortex flow pancake (VFP). The most promising bio-wax was identified in the beeswax-carnauba blend, the bWD. The bWD exhibits intermediate behavior between the beeswax and the carnauba. The bWD formulation shows good compromise in terms of thermal, structural, and ballistic properties. The exceptionally stiff and stronger, but brittle behavior of carnauba is balanced with the beeswax, which also increases the regression rate of the carnauba. The bWD formulation was used to embed the 3D-printed bio-polymeric reinforcements to create the eco-version of the armored grains. The considered armored grains featured 10% and 15% volume fractions (i.e. relative density or infill) for the inner gyroid armor. The mechanical and ballistic assessments of the armored grain were carried out.

The enhanced structural and burning characteristics of armored grain are found to be dependent on (i) the selected wax for the matrix (mwA or bWD), (ii) the material used to 3D print the gyroid reinforcement (ABS, NO, MB), and (iii) the infill fraction of the gyroid (10% or 15%). The stiffer and stronger armored grains are the ones based on the stiffer and stronger wax, i.e. the bWD. The same consideration holds for the polymer of the gyroid reinforcement. A higher volume fraction for the gyroid (15% rather than 10%) entails better mechanical properties (higher E and σ_y) but reduced r_f. All the investigated armored grains exhibit improved mechanical and ballistic properties than pure waxes. The 3D-printed reinforcements turned the extremely brittle behavior of the pristine natural waxes into a tough mechanical response, thus increasing the deformation energy. The firing tests revealed that the bio-armored grains burn faster than the natural wax baseline. The ballistic characterization via the VFP engine confirmed the same RBE trends. However, the exotic VFP configuration led to a lower r_f increase with respect to the conventional RBE.

The results of the present work indicate that the already promising armored grain concept can be further improved by proposing a "more-sustainable" version based on bio-wax and bio-polymer. The armored grain pushed the hybrid propulsion technology towards faster and tougher fuels; now, it is also possible to go greener. Firing tests in the VFP represent the starting point to prove the feasibility of armored grain for real flying systems. Even though the VFP implemented at SPLab has sizes and performances similar to those used in-space operations, firing tests on larger-scale HRE are needed. The armored grains exhibited a fast-burning behavior, but the combustion mechanism deserves additional and deeper studies. Numerical simulations, via computational fluid dynamics (CFD), would provide a better comprehension of the combustion mechanism in the different burning configurations of the RBE and the VFP.

References

[1] A. Okninski, W. Kopacz, D. Kaniewski, and K. Sobczak, "Hybrid rocket propulsion technology for space transportation revisited - propellant solutions and challenges," *FirePhysChem*, vol. 1, no. 4, pp. 260–271, 2021.

[2] D. Altman, "Overview and history of hybrid rocket propulsion," in *Fundamentals of Hybrid Rocket Combustion and Propulsion* (M. J. Chiaverini and K. K. Kuo, eds.), ch. 1, pp. 1–36, AIAA, 2007.

[3] C. Paravan, L. Galfetti, and F. Maggi, "A critical analysis of paraffin-based fuel formulations for hybrid rocket propulsion," in *53rd AIAA/SAE/ASEE Jt. Propuls. Conf.*, (Atlanta, GA), pp. 1–17, 2017.

[4] "Armored Grain by Riccardo Bisin - Hybrid Rocket Propulsion at SPLab." `https://youtu.be/Ll4SnVZ-6V0`. Accessed: 2023-06.

[5] R. Bisin, S. Alberti, A. Verga, C. Paravan, and L. Galfetti, "Green fuels for rocket propulsion: Current status and future perspectives of paraffin-based formulations," in *70th Int. Astronaut. Congr. (IAC)*, (Washington, DC), pp. 1–11, 2019.

[6] R. Bisin, C. Paravan, S. Alberti, and L. Galfetti, "A new strategy for the reinforcement of paraffin-based fuels based on cellular structures: The armored grain – mechanical characterization," *Acta Astronaut.*, vol. 176, pp. 494–509, 2020.

[7] R. Bisin and C. Paravan, "A new strategy for the reinforcement of paraffin-based fuels based on cellular structures: The armored grain – ballistic characterization," *Acta Astronaut.*, vol. 206, pp. 284–298, 2023.

[8] R. Bisin, C. Paravan, S. Parolini, and L. Galfetti, "Impact of 3D-printing on the mechanical reinforcement and the ballistic response of paraffin-based fuels: the armored grain," in *AIAA Propul. Energy 2020 Forum*, (Virtual Event), pp. 1–21, 2020.

[9] R. Bisin, C. Paravan, A. Verga, and L. Galfetti, "Towards high-performing paraffin-based fuels exploiting the armored grain concept," in *9th Eur. Conf. for Aeronaut. and Space Sci. (EUCASS)*, (Lille, FR), pp. 1–11, 2022.

[10] "Novamont website." `https://www.novamont.com/eng/`. Accessed: 2023-05.

[11] C. Paravan, L. Galfetti, R. Bisin, and F. Piscaglia, "Combustion processes in hybrid rockets," *Int. J. Energ. Mater. Chem. Propul.*, vol. 18, no. 3, pp. 255–286, 2019.

[12] M. Grosse, "Effect of a diaphragm on performance and fuel regression of a laboratory scale hybrid rocket motor using nitrous oxide and paraffin," in *45th AIAA/ASME/SAE/ASEE Jt. Propuls. Conf. Exhib.*, (Denver, CO), pp. 1–25, 2009.

[13] M. Kobald, E. Toson, H. Ciezki, S. Schlechtriem, S. Di Betta, M. Coppola, and L. De Luca, "Rheological, optical, and ballistic investigations of paraffin-based fuels for hybrid rocket propulsion using a two-dimensional slab-burner," in *Prog. Propuls. Phys.*, vol. 8, pp. 263–282, 2016.

[14] "Sasol website, products and applications, microcrystalline waxes." `http://www.sasolgermany.de/fileadmin/sasolwax/Personal_Care_Waxes_and_Petroleum_jellies.pdf`. Accessed: 2023-07.

[15] J. Scholes, "Bio-derived fuels for hybrid rocket motors," Master's thesis, University of Tennessee, 2005.

[16] S. Putnam, *Investigation of Non-Conventional Bio-Derived Fuels for Hybrid Rocket Motors*. PhD thesis, University of Tennessee, 2007.

[17] G. Saravanan, S. Shanmugam, and A. Veerappan, "Regression rate performance of paraffin wax and bees wax-gox with varied grain configuration in a hybrid rocket motor," *Aircr. Eng. Aerosp. Tec.*, vol. 93, no. 10, 2021.

[18] S. Mahottamananda, D. Kumar, A. Afreen, S. Dinesh, W. Ashiq, P. Kadiresh, and M. Thirumurugan, "Mechanical characteristics of ethylene vinyl acetate mixed beeswax fuel for hybrid rockets," in *Advances in Design and Thermal Systems*, pp. 389–401, 2021.

[19] S. Mahottamananda, "Beeswax-eva/activated-charcoal-based fuels for hybrid rockets: Thermal and ballistic evaluation," *Energies*, vol. 15, no. 20, p. 7578, 2022.

[20] "Food and Agriculture Organization of the United Nations (FAO) website, Carnauba Wax." `https://web.archive.org/web/20170807023631/http://www.fao.org/ag/agn/jecfa-additives/specs/Monograph1/Additive-109.pdf`. Accessed: 2023-09.

[21] S. A. Whitmore, Z. W. Peterson, and S. D. Eilers, "Comparing hydroxyl terminated polybutadiene and acrylonitrile butadiene styrene as hybrid rocket fuels," *J. Propul. Power*, vol. 29, no. 3, pp. 582–592, 2013.

[22] M. McFarland and E. Antunes, "Small-scale static fire tests of 3D printing hybrid rocket fuel grains produced from different materials," *Aerosp.*, vol. 6, no. 7, p. 81, 2019.

[23] C. Oztan and V. Coverstone, "Utilization of additive manufacturing in hybrid rocket technology: A review," *Acta Astronaut.*, vol. 180, pp. 130–140, 2021.

[24] P. Azimi, D. Zhao, C. Pouzet, N. E. Crain, and B. Stephens, "Emissions of ultrafine particles and volatile organic compounds from commercially available desktop three-dimensional printers with multiple filaments," *Environ. Sci. Technol.*, vol. 50, no. 3, pp. 1260–1268, 2016.

[25] "Prusa website, filament ASA/ABS." `https://shop.prusa3d.com/en/filament/134-orange-easyabs-filament-1kg.html`. Accessed: 2023-06.

[26] "Filamentum website." `https://www.fillamentumnonoilen.com`. Accessed: 2023-06.

[27] J. Ackermann, S. Muller, A. Losche, T. Bley, and W. Babel, "Methylobacterium rhodesianum cells tend to double the dna content under growth limitations and accumulate phb," *Journal of Biotechnology*, vol. 1, pp. 9–20, 1995.

[28] "Felfil website." `https://felfil.com/`. Accessed: 2023-05.

[29] R. Bisin, A. Verga, D. Bruschi, and C. Paravan, "Strategies for paraffin-based fuels reinforcement: 3d printing and blending with polymers," in *AIAA Propul. Energy 2021 Forum*, (Virtual Event), pp. 1–20, 2021.

[30] W. W. Wendlandt, *Thermal methods of analysis*. New York, Wiley-Interscience, second ed., 1974.

[31] R. B. Prime, H. E. Bair, S. Vyazovkin, P. K. Gallagher, and A. Riga, "Thermogravimetri analysis (TGA)," in *Thermal Analysis of Polymers* (J. D. Menczel and R. B. Prime, eds.), ch. 3, pp. 241–317, John Wiley and Sons, Ltd, 2008.

[32] Int. Organ. Stand., "ISO 604:2002 Plastics - Determination of compressive properties." `https://www.iso.org/standard/31261.html`.

[33] T. Marquardt and J. Majdalani, "Review of classical diffusion-limited regression rate models in hybrid rockets," *Aerosp.*, vol. 6, no. 6, p. 75, 2019.

[34] M. A. Karabeyoglu, G. Zilliac, B. J. Cantwell, S. DeZilwa, and P. Castellucci, "Scale-up tests of high regression rate paraffin-based hybrid rocket fuels," *J. Propul. Power*, vol. 20, no. 6, pp. 1037–1045, 2004.

[35] V. Santolini, R. Bisin, F. Giambelli, and C. Paravan, "An overview of SPLab activities on vortex combustion in a non-conventional hybrid rocket engine," in *13th Int. Symp. Spec. Top. Chem. Propul. Energ. Mater. (13-ISICP)*, (Gjovik, NO), 2023.

[36] S. No Lee, M. Yeon Lee, and W. Ho Park, "Thermal stabilization of poly(3-hydroxybutyrate) by poly(glycidyl methacrylate)," *J. Appl. Polym. Sci.*, vol. 83, pp. 2945–2952, 2002.

[37] P. Cerruti, G. Santagata, G. Gomez d'Ayala, V. Ambrogi, C. Carfagna, M. Malinconico, and P. Persico, "Effect of a natural polyphenolic extract on the properties of a biodegradable starch-based polymer," *Polymer Degradation and Stability*, vol. 96, pp. 839–846, 2011.

[38] M. P. Arrieta, D. Lopez, J. Lopez, J. Kenny, and L. Peponi, "Development of flexible materials based on plasticized electrospun pla-phb blends: Structural, thermal, mechanical and disintegration properties," *European Polymer Journal*, vol. 73, pp. 433–446, 2015.

[39] A. Hashish, C. Paravan, R. Bisin, and C. Scatton, "Ballistic characterization of armored grains with vortex flow pancake hybrid rocket engine," in *AIAA SCITECH 2023 Forum*, (National Harbor, MD and Online), pp. 1–15, 2023.